AIP Physics of Plasmas

# Helicon thruster plasma modeling: Two-dimensional fluid-dynamics and propulsive performances

Eduardo Ahedo and Jaume Navarro-Cavallé

Citation: Phys. Plasmas 20, 043512 (2013); doi: 10.1063/1.4798409
View online: http://dx.doi.org/10.1063/1.4798409
View Table of Contents: http://pop.aip.org/resource/1/PHPAEN/v20/i4
Published by the American Institute of Physics.

PHYSICS OF PLASMAS **20**, 043512 (2013)

# Helicon thruster plasma modeling: Two-dimensional fluid-dynamics and propulsive performances

Eduardo Ahedo[a)] and Jaume Navarro-Cavallé
*ETS Ingenieros Aeronáuticos, Universidad Politécnica de Madrid, Madrid 28040, Spain*

(Received 16 January 2013; accepted 7 March 2013; published online 17 April 2013)

An axisymmetric macroscopic model of the magnetized plasma flow inside the helicon thruster chamber is derived, assuming that the power absorbed from the helicon antenna emission is known. Ionization, confinement, subsonic flows, and production efficiency are discussed in terms of design and operation parameters. Analytical solutions and simple scaling laws for ideal plasma conditions are obtained. The chamber model is then matched with a model of the external magnetic nozzle in order to characterize the whole plasma flow and assess thruster performances. Thermal, electric, and magnetic contributions to thrust are evaluated. The energy balance provides the power conversion between ions and electrons in chamber and nozzle, and the power distribution among beam power, ionization losses, and wall losses. Thruster efficiency is assessed, and the main causes of inefficiency are identified. The thermodynamic behavior of the collisionless electron population in the nozzle is acknowledged to be poorly known and crucial for a complete plasma expansion and good thrust efficiency. © *2013 American Institute of Physics*. [http://dx.doi.org/10.1063/1.4798409]

## I. INTRODUCTION

The helicon plasma thruster (HPT) is an innovative technology for space propulsion, which, at present, is being researched extensively.[1–7] The device is constituted of a helicon source, where the plasma is generated and heated, and an external divergent magnetic nozzle, where the plasma is accelerated. The physical elements of a HPT are: a cylindrical dielectric chamber; a gas injection system, usually at the back of the chamber; an external antenna wrapped around the chamber and emitting rf waves, typically in the range 1-26 MHz, which propagate within the plasma; and a set of magnetic coils (or permanent magnets) that creates a longitudinal magnetic field, typically in the range $10^2$ to $10^3$ Gauss. In the "conventional" design, the magnetic field is predominantly axial inside the chamber and divergent outside it, and has several roles. First, it makes the plasma column transparent to the propagation of the rf emission as helicon waves. Second, the magnetic field screens the chamber walls, thus reducing greatly plasma losses at them.[8] Third, outside the chamber, the divergent magnetic topology creates a magnetic nozzle that channels the supersonic plasma flow, transforming the plasma internal energy into axially directed one, in a process very similar to the expansion of a hot gas in a conventional solid nozzle.[9,10]

The typical operation range of helicon sources is[11] $\omega_{lh} \ll \omega \ll \omega_{ce} \ll \omega_{pe}$, with $\omega_{lh}$ the lower-hybrid frequency, $\omega$ the wave frequency, $\omega_{ce}$ the electron cyclotron frequency, and $\omega_{pe}$ the plasma frequency. Helicon waves pertain to the branch of whistler waves; in a cold, unbounded plasma, no other waves can propagate in that frequency range.[12] Although a unique theory for the absorption of the energy of helicon waves is not fully established yet, the plausible collisional theory, for dense enough plasmas, states that absorption is achieved through the mediation of Trivelpiece-Gould surface waves, which are highly dissipative.[11,13] The advantage of helicon sources over other rf sources (such as inductively coupled ones) is that, adjusting conveniently the magnetic intensity ($\omega_{ce} \propto B$), there is not a severe cut-off of plasma density for wave propagation, and values of $10^{18} - 10^{20}\,\mathrm{m}^{-3}$ are achievable.[14]

Other potential advantages of the HPT for space propulsion would be: the lack of electrodes, thus avoiding erosion limitations and promising a long thruster lifetime; the capability of operating with a wide range of propellants;[1,15] and high throttlability, based on the capability of actuating, at constant power, on both the gas flow and the magnetic nozzle.[16] However, existing HPT prototypes are still far from achieving propulsive figures capable of competing with other mature plasma thrusters. For instance, thrust efficiency is below 5% in the few cases were it has been measured directly.[17–19] In this context, the understanding of the multiple physical processes taking place in the HPT, the interplay among them, and the assessment of HPT performances are much needed.

A complete model of the HPT must deal with both the plasma-wave interaction and the fluid-dynamics of the plasma discharge. The two processes, although strongly coupled, require well differentiated models. This paper deals exclusively with the fluid-dynamics problem and assumes that the plasma column has absorbed a known amount of rf energy in the form of electron internal energy. In turn, the analysis of the plasma flow distinguishes between the chamber/internal and the nozzle/external regions. An axisymmetric model for the external region was already derived in Ref. 10 and was applied to discuss the 2D supersonic plasma expansion, the development of electric currents in the plasma, and the magnetic thrust mechanism. Posterior work on the nozzle region has advanced on the plasma/nozzle detachment issue[20–22] and the formation of double-layer type

[a)]Electronic mail: eduardo.ahedo@upm.es; URL: web.fmetsia.upm.es/ep2/

 

of structures.[23–25] The present paper has two main goals: first, to develop an axisymmetric model of plasma fluid-dynamics inside the chamber, and second, to match it to the nozzle model in order to evaluate HPT performances in terms of thrust, useful energy, and thrust efficiency.

The first part of the paper derives the axisymmetric model of the chamber and analyzes plasma generation, heating, wall interaction, and internal flows. The model is based on decoupling partially the radial and axial dynamics through an approximate variable-separation technique, already applied successfully to the plasma discharge in a Hall thruster;[26] the main coupling parameter between axial and radial dynamics is the local wall-recombination frequency. Fruchtman *et al.*[27] were the first to apply the variable-separation technique to the 2D study of the plasma flow inside the chamber of a HPT. Our chamber model recovers, of course, part of theirs but, at the same time, completes or modifies the following central aspects of theirs: (a) the neutral density was taken constant [in a subsequent paper, Fruchtman[28] discussed neutral depletion within a 1D chamber model, still ignoring plasma recombination at the chamber wall], (b) radial plasma dynamics were purely diffusive; (c) ion dynamics were dominated by collisionality; and (d) a closed energy balance within the chamber was attained by assuming an adiabatic electron energy flow at the chamber exit.

Thus, central to our model will be to include the 2D depletion of the injected gas flow, which is governed by the competition between plasma volumetric-production and wall-recombination, the amount of this last one depending mainly on the magnetic screening of the walls. Then, the radial dynamics will show the formation of a quasineutral inertial region between the bulk diffusion region and the lateral Debye sheath, with effects on the lateral deposition of energy. Regarding the ion dynamics and for typical helicon source conditions, ions will be found to be both weakly collisional and weakly magnetized, and their free motion will be governed by the 2D ambipolar electric field. Finally, it will shown that, in general, the energy balance on the magnetized electron population requires to take into account both the internal and external dynamics.

Apart from deriving the chamber model and computing exact solutions, our study of the chamber region offers two additional contributions. First, asymptotic regimes of the radial and axial dynamics are presented. These are highly valuable, since they provide both the clearest insight of the relevant internal physics and useful scaling laws relating the plasma response to operational and design parameters. Second, a parametric investigation is carried out, aiming at determining the way to maximize plasma production efficiency.

The second part of the paper is devoted to evaluate thruster performances. This requires first to match the 2D chamber model to the 2D magnetic-nozzle model of Ref. 10. Both models have been developed independently and involve assumptions and techniques suitable to the respective plasma conditions. This is going to produce a small mismatching between the internal and external solutions at the vicinity of the mutual interface (i.e., around the chamber exit) with marginal effect on the consistency of results and conclusions.

Thruster performances will be analyzed in terms of both thrust (i.e., plasma momentum) and energy. The different contributions to thrust are evaluated. Partial efficiencies will be defined in order to assess the relevance of the different physical processes (such as ionization, wall losses, and plume divergence) on the thrust efficiency. The electron energy behavior will be shown to be central for the plasma response in the nozzle and the thrust efficiency.

The rest of the paper is organized as follows. Section II presents the 2D chamber model. Section III discusses the plasma response inside the chamber. Section IV matches the chamber and nozzle models and discusses the different contributions to thrust. Section V presents the energy balance and discusses thrust efficiency. Section VI is for conclusions.

## II. FORMULATION OF THE CHAMBER MODEL

Figure 1 sketches the HPT, with the chamber and nozzle regions and an example of magnetic topology created by a Maxwell 3-coil arrangement. The magnetic field is nearly axial inside the chamber (to the left of the third coil), and divergent at the nozzle. The rectangle symbolizes the elongated cylindrical chamber of radius $R$ and length $L$. Let A, W, and E be the chamber back-wall, lateral, and front-exit, respectively. The magnetic field inside the chamber is approximated as purely axial and constant, $\boldsymbol{B} = B_0 \boldsymbol{1}_z$.

A mass flow $\dot{m}$ of neutral gas is injected at the cylinder back-wall (where we set $z_A = -L$) and is ionized by impact of electrons. In steady-state operation, we assume that electrons have been energized by the rf emission, acquiring a steady-state, uniform temperature $T_e$. The resulting plasma is constituted of singly charged ions, electrons, and neutrals (subscripts $i$, $e$, and $n$, respectively). Plasma density is, on the one side, high enough for assuming the zero-Debye-length limit and, on the other side, low enough for assuming the zero-beta limit and thus neglect the induced magnetic field.[29] Thereby, the plasma is quasineutral with $n \equiv n_e = n_i$ except in Debye sheaths around the chamber walls, which constitute surface discontinuities in the quasineutral scale. Thus, the sonic Bohm criterion applies to the perpendicular flow at the edges, B and Q, of the back and lateral sheaths respectively (Fig. 1). The perpendicular flow is also assumed sonic at the chamber exit section E (where we set $z_E = 0$).

Continuity and momentum equations for each species ($j = i, e, n$) are

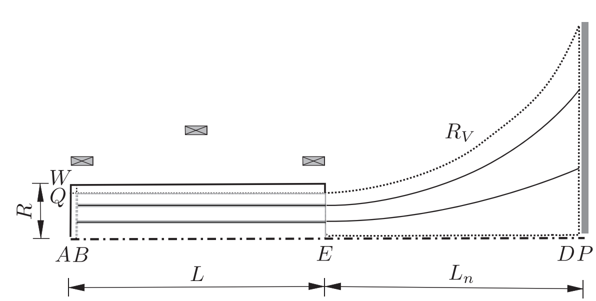


FIG. 1. Sketch of the model (not done to scale).

$$\nabla \cdot (n_e \boldsymbol{u}_e) = \nabla \cdot (n_i \boldsymbol{u}_i) = -\nabla \cdot (n_n \boldsymbol{u}_n) = n_e n_n R_{ion}, \quad (1)$$

$$\nabla \cdot (m_j n_j \boldsymbol{u}_j \boldsymbol{u}_j) = -\nabla p_j + q_j n_j (-\nabla \phi + \boldsymbol{u}_j \times \boldsymbol{B}) - \boldsymbol{S}_j, \quad (2)$$

where $m_j$ is particle mass and $q_j$ is electric charge (with $q_e = -e$ for electrons); $\boldsymbol{u}_j$ is macroscopic velocity, $n_j$ is density, and $p_j = T_j n_j$ is pressure; $\phi$ is the ambipolar electric potential, and $\boldsymbol{S}_j$ groups different collisional processes on each species. These include ionization and elastic electron-neutral, electron-ion, and ion-neutral collisions, with subindexes *ion*, *en*, *ei*, and *in*, respectively. Collisional rates for these processes, $R_k$ ($k = ion, en, ei, in$), are defined in the Appendix and plotted in Fig. 2 in terms of $T_e$.

According to the analyses of Refs. 8, 26, and 27, and for a chamber with $L \gg R$, the following assumptions and conventions are adopted for the in-chamber model:

(1) Axial symmetry: $\partial/\partial\theta = 0$.
(2) Neutrals are assumed cold, with $\boldsymbol{u}_n = u_n \boldsymbol{1}_z$, and their density and velocity depend only on $z$. (These simplifications are well justified for a magnetized plasma with small wall recombination.)
(3) Ion pressure is much smaller than electron pressure.
(4) The plasma current $\boldsymbol{j}$ satisfies the longitudinal ambipolarity condition $\boldsymbol{j} - \boldsymbol{1}_\theta j_\theta = \boldsymbol{0}$, yielding $u_{ri} = u_{re} \equiv u_r$ and $u_{zi} = u_{ze} \equiv u_z$. (This is rather plausible for an elongated dielectric chamber.)
(5) Plasma density is expressed as

$$n(z, r) = n_z(z) n_r(z, r),$$

with $(2/R^2)\int_0^R r n_r(z, r) dr = 1$ for all $z$.
(6) The electric potential is split as

$$\phi(z, r) = \phi_z(z) + \phi_r(z, r),$$

with $\phi_r(z, 0) = 0$ for all $z$.
(7) $u_{\theta i} \ll u_{\theta e} \equiv u_\theta$, so that magnetic effects on ions are negligible.
(8) Longitudinal electron-inertia is negligible, but azimuthal electron-inertia (due to $u_\theta$) is retained.
(9) Spatial gradients satisfy the following orderings:

$$\partial n_r/\partial z \ll \partial n_r/\partial r, \quad \partial \phi_r/\partial z \ll \partial \phi_r/\partial r,$$

$$\partial(u_r, u_\theta)/\partial z \ll \partial(u_r, u_\theta)/\partial r, \quad \partial u_z/\partial r \ll \partial u_z/\partial z.$$

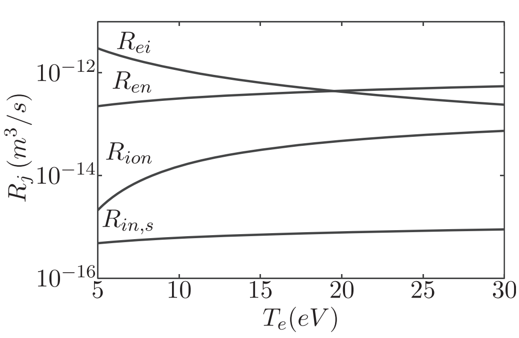


FIG. 2. Ionization and collision rates, $R_j(m^3/s)$, for $j = ei, en, ion$, and $in$. $R_{in,s}$ is $R_{in}$ for $c_{in} = c_s$.

These assumptions reduce the 2D model into axial and radial models coupled mainly through the wall recombination frequency $\nu_w(z)$, which is an eigenfunction to be determined. Then, the axially dependent equations are

$$n_z u_z + n_n u_n = g_0, \quad (3)$$

$$\frac{\partial}{\partial z}(n_z u_z) = n_z(n_n R_{ion} - \nu_w), \quad (4)$$

$$u_z \frac{\partial u_z}{\partial z} = -c_s^2 \frac{\partial \ln n_z}{\partial z} - n_n(R_{in} + R_{ion})(u_z - u_n), \quad (5)$$

$$u_n \frac{\partial u_n}{\partial z} = -n_z \left[ R_{in}(u_n - u_z) + \frac{\nu_w}{n_n} u_n (1 - \alpha_w) \right], \quad (6)$$

$$e \frac{\partial \phi_z}{\partial z} = T_e \frac{\partial \ln n_z}{\partial z}. \quad (7)$$

Here, $c_s = \sqrt{T_e/m_i}$ is the sound velocity, $g_0 = \dot{m}/(m_i \pi R^2)$ is the (constant) axial flux of heavy species (i.e., ions and neutrals), and $\alpha_w u_n$ is an effective axial velocity of neutrals created from plasma recombination at the lateral wall.

The radially dependent equations are[8]

$$\frac{1}{r}\frac{\partial}{\partial r}(r n_r u_r) = n_r \nu_w, \quad (8)$$

$$u_r \frac{\partial u_r}{\partial r} = -c_s^2 \frac{\partial \ln n_r}{\partial r} - \frac{eB_0}{m_i} u_\theta + \frac{m_e}{m_i}\frac{u_\theta^2}{r} - n_n(R_{in} + R_{ion}) u_r, \quad (9)$$

$$u_r \frac{\partial u_\theta}{\partial r} = \frac{eB_0}{m_e} u_r - [n_n(R_{en} + R_{ion}) + n_r R_{ei}] u_\theta - \frac{u_\theta u_r}{r}, \quad (10)$$

$$e \frac{\partial \phi_r}{\partial r} = T_e \frac{\partial \ln n_r}{\partial r} + eB_0 u_\theta - m_e \frac{u_\theta^2}{r}. \quad (11)$$

Therefore, the axial model determines the set $(n_z, n_n, u_z, u_n, \phi_z)$, which depends only on $z$, while the radial model yields, at each $z$, the set $(n_r, u_r, u_\theta, \phi_r)$. Notice that equations for $\phi_z$ and $\phi_r$ are decoupled from the rest.

### A. The radial model

The radial model is discussed in detail in Ref. 8. Dimensionless variables are $r/R$, $n_r/n_r(z, 0)$, $e\phi_r/T_e$, $u_r/c_s$, and $u_\theta/c_e$, with $c_e = \sqrt{T_e/m_e}$ used for non-dimensionalizing $u_\theta$ instead of $c_s$. Boundary conditions at $r = 0$ are

$$u_r = u_\theta = \ln[n_r/n_r(z, 0)] = \phi_r = 0.$$

The extra condition $u_r = c_s$ at $r = R$ (i.e., the Bohm criterion at the sheath edge) determines the eigenvalue $\nu_w(z)$ in the functional form

$$\frac{\nu_w}{\omega_r} = \hat{\nu}_w \left( \frac{\omega_{lh}}{\omega_r}, \frac{\nu_{ion}}{\omega_r}, \frac{\nu_{en}}{\omega_r}, \frac{\nu_{ei0}}{\omega_r} \right) \quad (12)$$

with $\omega_r = c_s/R$ (the radial-transit frequency), $\omega_{lh} = eB_0/\sqrt{m_e m_i}$, $\nu_{ei0} = (R_{ei} n)_{r=0}$, $\nu_{en} = R_{en} n_n$, and $\nu_{ion} = R_{ion} n_n$; ion-neutral collisions are negligible in the regimes of interest here.

Reference 8 showed that the main magnetized regime corresponds to

$$\omega_{lh} \gg \nu_{en} + \nu_{ei} + \nu_{ion} + \nu_{in} \geq O(\omega_r).$$

Notice that the magnetized plasma condition $\omega_r/\omega_{lh} \ll 1$ is equivalent to $\ell_e/R \ll 1$, with $\ell_e$ the electron Larmor radius. In the magnetized regime, the radial structure of the plasma column consists of a bulk diffusive region, a thin inertial layer (quasineutral and collisionless), and the thinner Debye sheath. For $\nu_e \equiv \nu_{en} + \nu_{ei} + \nu_{ion} = \text{const}$, the asymptotic universal solution for the bulk region is[30]

$$\frac{n_r(z,r)}{n_r(z,0)} = J_0\left(a_0\frac{r}{R}\right), \quad \frac{u_r}{c_s} = a_0\frac{\nu_e\omega_r}{\omega_{lh}^2}\frac{J_1(a_0r/R)}{J_0(a_0r/R)}, \quad \frac{u_\theta}{c_e} = \frac{u_r}{c_s}\frac{\omega_{lh}}{\nu_e}, \tag{13}$$

the inertial layer covers the range $u_r/c_s \sim \nu_e/\omega_{lh}$ to $u_r/c_s = 1$; and the plasma balance condition, Eq. (12), reduces asymptotically to

$$\nu_w = a_0^2\frac{\omega_r^2}{\omega_{lh}^2}\nu_e, \tag{14}$$

with $a_0 \simeq 2.405$, the first-zero of the Bessel function of the first kind $J_0$.

## B. The axial model

After some manipulation, the set of Eqs. (3)–(7) yields

$$(c_s^2 - u_z^2)\frac{\partial u_z}{\partial z} = (u_z - u_n)u_z n_n(R_{in} + R_{ion}) + c_s^2(n_nR_{ion} - \nu_w), \tag{15}$$

$$(c_s^2 - u_z^2)\frac{\partial n_z}{\partial z} = -n_z[u_z(n_nR_{ion} - \nu_w) - (u_z - u_n)n_n(R_{in} + R_{ion})], \tag{16}$$

$$n_nu_n\frac{\partial u_n}{\partial z} = n_z[u_n\nu_w(\alpha_w - 1) + (u_z - u_n)n_nR_{in}]. \tag{17}$$

Boundary conditions for these equations are imposed at the back-wall sheath edge B and the front exit E

$$g_0 \text{ known}, \quad u_{nB} = u_{n0}, \quad u_{zB} = -c_s, \quad u_{zE} = c_s.$$

Non-dimensionalization with $c_s$, $g_0$, and $L$ yields that the axial solution depends on the following dimensionless parameters:

$$L/L_\star, \quad R_{in,s}/R_{ion}, \quad u_{n0}/c_s, \quad \alpha_w,$$

plus the eigenfunction $\nu_w/(n_nR_{ion})$. Here,

$$L_\star = c_s/(R_{ion}n_{n0})$$

is an effective ionization mean-free-path, quotient of the scaled ionization cross section $R_{ion}/c_s$ (which depends only on $T_e$), and the neutral density $n_{n0} = g_0/u_{n0}$.

For efficient thruster operation, $T_e$ and $B_0$ must be large enough to have

$$\nu_w/(n_nR_{ion}) \ll 1, \quad R_{in,s}/R_{ion} \ll u_{n0}/c_s \ll 1,$$

and (for $\alpha_w = 1$) the axial plasma flow admits the *ideal* (or perfect confinement) solution

$$u_n = u_{n0}, \quad \frac{u_z}{c_s} = \tan\xi, \quad \frac{n}{n_0} = 2\eta_u\cos^2\xi, \quad \frac{n_n}{n_{n0}} = 1 - \eta_u\sin 2\xi, \tag{18}$$

$$\frac{z + L}{L_\star} = \int_{-\pi/4}^{\xi}\frac{1 - \tan^2\xi'}{1 - \eta_u\sin 2\xi'}d\xi', \tag{19}$$

where $n_0 = g_0/c_s$ is a reference plasma density, $\xi$ is an auxiliary variable, and $\eta_u = n_E/n_0$ coincides with the propellant utilization. Setting $z = 0$ at $\xi = \pi/4$ in Eq. (19) yields implicitly the relation $\eta_u(L/L_\star)$

$$\frac{L}{L_\star} = \int_{-\pi/4}^{\pi/4}\frac{1 - \tan^2\xi}{1 - \eta_u\sin 2\xi}d\xi. \tag{20}$$

Although the functions in Eq. (18) are symmetric with respect to $\xi$, the function $z(\xi)$ is not symmetric, the point $\xi = 0$ (where $u_{zi} = 0$ and $n$ is maximum) being shifted towards the chamber rear wall.

# III. PLASMA RESPONSE INSIDE THE CHAMBER

This section discusses the 2D spatial solution and the resulting performances of the plasma inside the chamber, in terms of the three main operation parameters: the magnetic field $B_0$, the gas flow $\dot{m}$, and the plasma temperature $T_e$ (which will be later related to the absorbed power $P_a$). Although the discussion can be done in terms of dimensionless parameters, for sake of clarity, we have opted for presenting dimensional results. Thus, we consider a cylindrical chamber with $R = 1$ cm and $L = 10$ cm, operating nominally with argon, $B_0 = 600$G, $\dot{m} = 0.1$ mg/s, and $T_e = 10$ eV. We also take $\alpha_w = 1$ and $u_{n0}/c_s = 0.07$. For these conditions, the typical values of dimensionless parameters are $\omega_{lh}/\omega_r = 80$, $\nu_{en}/\omega_r \sim 10$, $\nu_{ei}/\omega_r \sim 3$, $\nu_w/n_nR_{ion} \sim 0.2$, $R_{in,s}/R_{ion} = 0.04$, and $L/L_\star = 3.7$.

## A. 2D plasma profiles

Figure 3 plots profiles of main axial magnitudes for two magnetic intensities, 200G and 600G, and compare them with the ideal axial solution of Eqs. (18) and (19). Fig. 4 plots profiles of two radial magnitudes at the chamber rear wall ($z = -L$) and front exit ($z = 0$), for the same magnetic intensities, and compare them with the ideal radial solution of Eq. (13).

Figure 3(a) shows how the injected neutral flow is effectively depleted by ionization. In Fig. 3(b), we observe that the plasma density presents a positive gradient at the back of the chamber, caused by ionization, and then, a negative gradient, caused by ion acceleration. Fig. 3(c) shows the region of backward and forward plasma flow, with $u_{zi} = 0$ marking also the location of the maximum $n_z$. Observe that the ion back-streaming region occupies only a small part of the chamber; in contrast, the constant-$n_n$ model of Ref. 27 yields

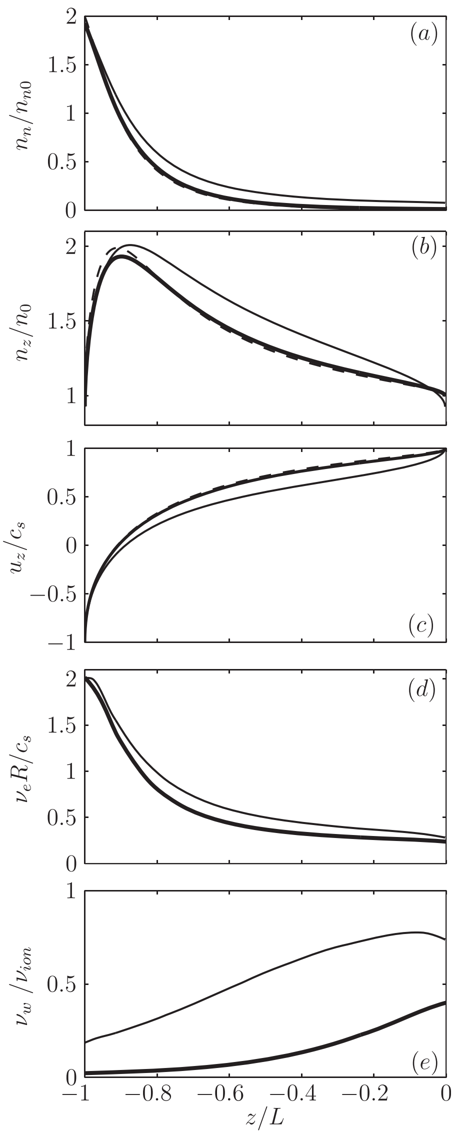


FIG. 3. Dimensionless axial profiles inside the chamber of (a) neutral density, (b) plasma density, (c) plasma velocity, (d) radially averaged electron collision frequency, and (e) plasma recombination-to-ionization ratio. Solid lines are for $B_0 = 600$G (thick) and 200G (thin), and dashed lines are for the ideal axial solution. Normalization constants are defined in the main text.

symmetric profiles of axial variables around the chamber mid-section, $z = -L/2$. Figure 3(d) plots the effective electron-collision frequency, which decreases by a factor of 8 between the chamber back and front sections, because of the decrease of $\nu_{en}$ ($\nu_{en} \propto n_n$). As a consequence, the plasma is more magnetized near the chamber exit, which affects the radial profiles of Fig. 4 and the local wall recombination. In fact, electron collisionality is dominated by collisions with neutrals, near the back wall, and with ions, near the front exit. Figure 3(e) depicts the ratio between wall-recombination and ionization along the chamber, which characterizes the net plasma production along the chamber. Wall-recombination is moderate for 200G and small for 600G, which explains why the ideal axial solution [dashed line in Figures 3(a)–3(c)] is almost indistinguishable from the exact 600 G-solution.

The radial profiles plotted in Fig. 4 do not cover the near-axis region $r/R < 0.4$, where gradients of $u_r$ are very

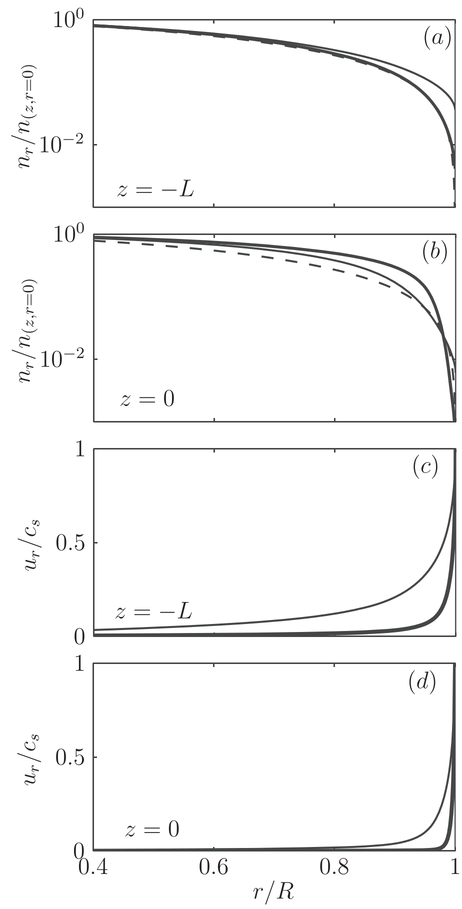


FIG. 4. Dimensionless radial profiles inside the chamber of ((a) and (b)) plasma density and ((c) and (d)) radial velocity $u_r/c_s$, at ((a) and (c)) the rear wall, $z = -L$, and ((b) and (d)) the exit section, $z = 0$. Solid lines are for $B_0 = 600$G (thick) and 200G (thin), and dashed lines are for the ideal radial solution. Normalization constants are defined in the main text.

small for high magnetization. The agreement of the exact solution with the ideal radial solution is excellent for $B_0 = 600$G at the back-wall section. At the exit section, the dominance in $\nu_e$ of electron-ion collisions, which are proportional to the local plasma density, makes the radial profile more steepened than in the ideal solution. The profiles of $u_r$ illustrate how a large magnetic confinement prevents developing large perpendicular velocities until the very vicinity of the wall. The same is true for the radial electric field, $-e\phi_r \simeq m_i u_r^2/2$, which is negligible outside the thin inertial layer, of thickness $\ell_e$, preceding the Debye sheath.

Figures 5(a) and 5(b) plot, for 200G, $r$–$z$ contour maps of plasma density and velocity $u_i$. The constant-velocity lines are also good approximations for isopotentials. Plasma magnetization, even if moderate as here, tend to concentrate the gradients of the plasma flow around the lateral and rear walls of the chamber. Notice that the radial gradients of $n$ in the bulk region are sustained not by the tiny radial electric field but by the radial magnetic force generated by the azimuthal electron current. At the chamber exit, the plasma beam is radially nonuniform and near-sonic.

If magnetic confinement is not large, plasma losses to the lateral wall are not negligible, and the fraction of neutrals created from recombination is significant. These are injected back into the plasma with a lower energy than the

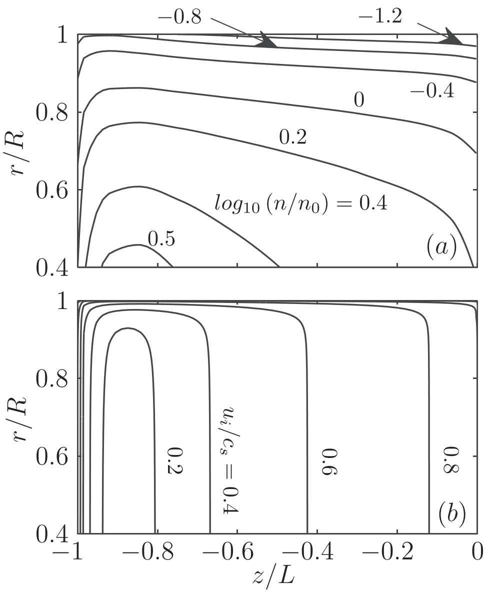


FIG. 5. Two-dimensional maps inside the chamber of plasma (a) density and (b) velocity, for $B_0 = 200$G.

recombined ions (a process known as accommodation) and not specularly, thus increasing the neutral thermal energy. Within our model framework, this neutral "heating" cannot be reproduced accurately but still we can estimate the sensitivity of the solution to the properties of recombined neutrals by varying the parameter $\alpha_w$ in Eq. (17). Figure 6 compares the solution for three cases: $\alpha_w = 1$, which keeps $u_n$ almost constant; $\alpha_w = 0$, which assumes that neutrals from recombination are injected back with zero energy; and $\alpha_w = 2$, which assumes that new neutrals keep some of the ion axial directed energy before recombination. Although the macroscopic neutral velocity is affected by recombination conditions, the profiles of plasma density (as well as other magnitudes) remain practically unaffected.

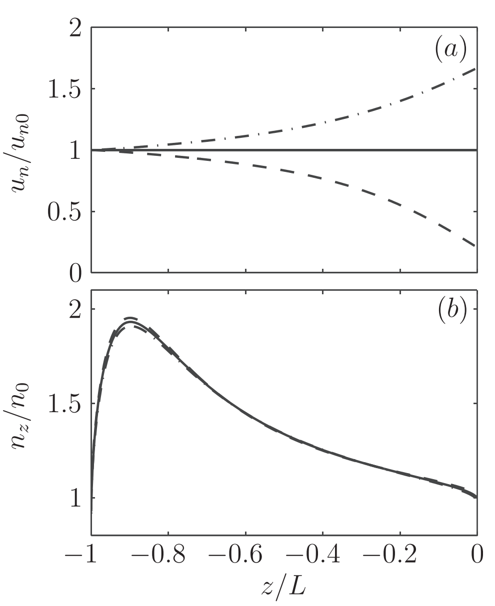


FIG. 6. Axial profiles inside the chamber of neutral (a) velocity and (b) density, for different values of the re-emission velocity parameter: $\alpha_w = 1$ (solid), 0 (dashed), and 2(dotted-and-dashed).

## B. Chamber performance parameters

The two main parameters characterizing plasma production in the chamber are the *propellant utilization* and the *production efficiency*, defined, respectively, as

$$\eta_u = \frac{\dot{m}_{iE}}{\dot{m}}, \qquad \eta_p = \frac{\dot{m}_{iE}}{\dot{m}_{iT}}, \tag{21}$$

where

$$\dot{m}_{iT} = \dot{m}_{iE} + \dot{m}_{iA} + \dot{m}_{iW}$$

is the total ion production rate in the chamber. This production is the sum of the ion mass flows at the chamber exit E, the back wall A, and the lateral wall W,

$$\dot{m}_{iE} = m_i \pi R^2 c_s n_E, \quad \dot{m}_{iA} = \dot{m}_{iB} = m_i \pi R^2 c_s n_B,$$
$$\dot{m}_{iW} = m_i 2\pi R \int_{-L}^{0} dz (n u_r)_{r=R},$$

respectively.

In the perfect confinement limit, the ideal law $\eta_u(L/L_\star)$, Eq. (20), plotted in Fig. 7(a), is indeed the scaling law for the propellant utilization in terms of $L$, $n_{n0}$, and $T_e$. The high propellant utilization regime requires $L/L_\star$ be large; for instance $L/L_\star \geq 2.5$ yields $\eta_u \geq 95\%$. Figure 7(b) plots the influence of a non-perfect confinement on $\eta_u$ for different plasma temperatures. For each $T_e$-curve, its knee separates a low-confinement, low-ionization regime from the high-ionization

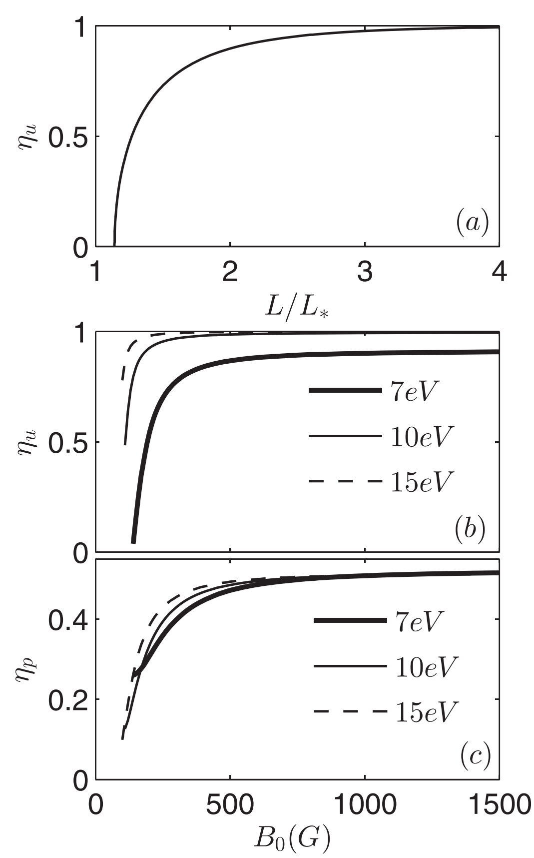


FIG. 7. Parametric investigation of chamber performances. (a) Ideal scaling law for propellant utilization. (b) Propellant utilization and (c) production efficiency, in terms of $B_0$ and $T_e$, for $\dot{m} = 0.1$ mg/s.

regime. As $\dot{m}$ is increased, the curves of Fig. 7(b) shift towards higher $\eta_u$ [see Fig. 8 below]. The achievement of high $\eta_u$ inside the chamber is mandatory for a plasma thruster to be competitive since outside the chamber the neutral density decreases and thus ionization drop quickly; in addition, downstream-produced ions acquire lower axial energy than in-chamber created ones.

The production efficiency $\eta_p$ measures the fraction of the produced plasma being ejected from the chamber and thus contributing efficiently to thrust. In the perfect confinement case and for a purely axial magnetic field, it would be $\dot{m}_W = 0$ and $\dot{m}_B = \dot{m}_E$, and the production efficiency would reach a meagre maximum of only 50%. Figure 7(c) plots the influence of $T_e$ and $B_0$ on $\eta_p$. The qualitative behaviour is similar to the case of $\eta_u$, with the curve knee separating the two regimes, and $\eta_p$ tending to the limit $\simeq$50% at high confinement. The production efficiency increases weakly with $T_e$ (due to a decrease of electron-ion collisionality).

Figures 8(a) and 8(b) plot parametric curves $\eta_u(B_0, \dot{m}) = \text{const}$ and $\eta_p(B_0, \dot{m}) = \text{const}$ for two values of $T_e$. They allow us to determine optimal values of $B_0$ and $\dot{m}$ and to assess the sensitivity of plasma production to these parameters. Notice that a high $\eta_u$ requires minimum values of $B_0$ and $\dot{m}$. Additionally, if we want to keep $\eta_p$ close to its maximum of 50%, the optimal values of $B_0$ and $\dot{m}$ are near the knee of the curve $\eta_u(B_0, \dot{m}) = \text{const}$, which is also the region less sensitive to changes on the operational parameters. As $T_e$ increases, the optimal values of $B_0$ and $\dot{m}$ decrease. Notice that for $B_0 = \text{const}$ and $\dot{m}$ increasing, $\eta_u$ increases but $\eta_p$ decreases.

Screening of the lateral wall by the axial magnetic field has been shown to make losses there negligible. At the same time, the lack of magnetic screening at the rear wall penalizes strongly $\eta_p$ and thus thruster performances. The penalty is due to the plasma flow to the rear-wall being similar to the front-exit one and requiring re-ionization. This large loss would be avoided by screening the back wall too. Magnetic screening of both the rear and lateral chamber walls is feasible by appropriate design of the magnetic circuit (via either coils or permanent magnets) but redounds in a 2D magnetic topology, which again cannot be treated accurately within our model framework. Nonetheless, a quantitative assessment can be made for the limit of *large local* screening of the rear wall, by just assuming that the plasma backflow to that wall is negligible. This implies to impose the boundary condition $u_z(-L) = 0$ instead of $u_z(-L) = -c_s$. Figure 9(a) shows that the maximum density is at the back wall, indicating that the forward-flow region $u_z > 0$ occupies the whole chamber. Since for a non-screened back wall, the back-streaming region was already short, the global changes on the 2D plasma response are small, but, as Fig. 9(b) confirms, screening of the rear-wall typically doubles the production efficiency, which can now approach 100%.

## IV. THRUST

### A. Matching chamber and nozzle models

The 2D chamber model can be matched now to the 2D divergent nozzle model of Ahedo and Merino.[31] This model assumes a collisionless, non-subsonic plasma, which fits well with the plasma exiting the chamber if, as desired, $\eta_u \approx 1$, and the plasma is hot (say $T_e > 10$ eV). Still there is a mismatching between the two models, caused by the plasma flow not fulfilling a regular sonic transition at section E: at present, the chamber model ends with a singular sonic flow, and the nozzle model starts with a slightly supersonic flow (typically with a Mach number $\approx$1.01). An additional mismatching, caused by the limit $\ell_e/R = 0$ assumed in the nozzle model, is that the thin inertial layer next to the chamber lateral wall is neglected in the nozzle, which, in our computations, means a 2%-3% loss in mass flow. In total, we estimate that the two mismatchings yield an error below 5%. The shape of the wall-less magnetic nozzle, $r = R_V(z)$ with $R_V(0) = R$, sketched in Fig. 1, corresponds to the plasma/

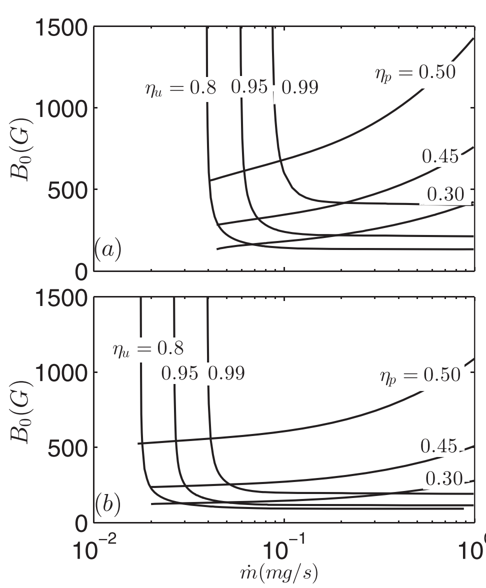


FIG. 8. Constant-level contours of propellant utilization and production efficiency in the parametric plane $\dot{m} - B_0$ for $T_e = 10$ eV (a) and 20 eV (b).

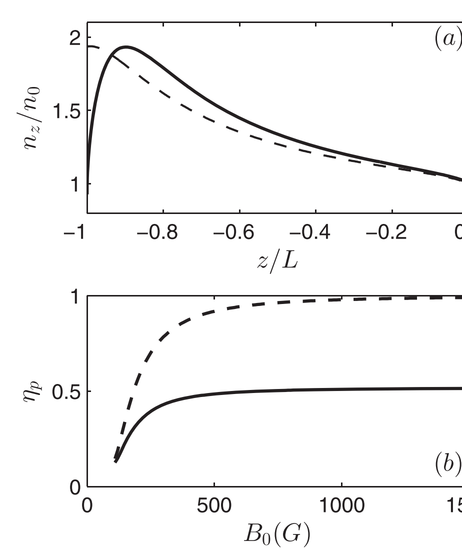


FIG. 9. Effects of magnetic screening of the back-wall: (a) Axial profile of plasma density and (b) production efficiency versus axial magnetic field. Solid and dashed lines are for $u_{zB}/c_s = -1$ and 0, respectively, modeling zero and total magnetic screening.

vacuum edge V. Two-dimensional profiles of the supersonic plasma expansion are discussed in Ref. 10.

At present, the nozzle model cannot be extended into the far-downstream region because two important issues, the plasma/nozzle detachment and the vanishing of the electric field, are not solved fully yet.[20,22] Thus, in order to close the problem in a reasonable way, an isolated (metallic) plate, represented by P in Fig. 1, will mark here the end of the nozzle region. The plate is located at a distance $L_n$ from the chamber exit and collects the plasma beam (without reinjecting it). Surface D in Fig. 1 is the edge of the Debye sheath developing in front the plate. Observe that the plate is not merely an artefact: it could model a material surface for processing,[32] a plasma momentum flux sensor for indirect thrust measurement,[33,34] or the downstream wall of the vacuum chamber.

Both $B_0$ and $\dot{m}$ have an important role on chamber performances, as we have shown before, but they have a lesser role on the plasma expansion in the near nozzle. Therefore, in this and Sec. V, $B_0$ and $\dot{m}$ are fixed to their nominal values of 600 G and 0.1 mg/s, and the discussion of thruster performances is focused on the influence of $T_e$ and the nozzle length $L_n$.

### B. Thrust contributions

Adding for the three species, the momentum flux equation of the whole plasma is

$$\nabla \cdot \bar{\bar{M}} = e(n_e - n_i)\nabla\phi - en_e\boldsymbol{u}_e \times \boldsymbol{B}, \tag{22}$$

where

$$\bar{\bar{M}} = \Sigma_{j=i,e,n}(m_j n_j \boldsymbol{u}_j\boldsymbol{u}_j + p_j\bar{\bar{I}})$$

is the plasma momentum flux tensor. The axial momentum flow across section $z = \text{const}$ is

$$F_z(z) = 2\pi\int_0^{R_V(z)} dr\, rM_{zz}(z,r) \tag{23}$$

with $R_V(z) = R$ inside the chamber.

Physically, the thrust $F$ is the net backwards force exerted by the whole plasma on the thruster. This (axial) force is the sum of three different contributions, namely,

$$F = F_{pres} - F_{elec} + F_{mag}. \tag{24}$$

Here,

$$F_{pres} = F_{zA} - D_W \tag{25}$$

is the axial dynamic pressure of the plasma at the chamber walls, with $F_{zA} = F_z(-L)$ and $D_W = \pi R^2 m_i\int_{-L}^0 dz\, n_z \nu_w(u_{zi} - \alpha_w u_n)$;

$$F_{elec} = \pi\epsilon_0\int_0^R dr\, r\left(\frac{d\phi}{dz}\right)_A^2 \tag{26}$$

is the axial electric force between the positive electric charge in the sheath AB and the negative electric charge at the back wall ($\epsilon_0$ is the vacuum dielectric permittivity); and

$$F_{mag} = 2\pi\int_0^{L_n} dz\int_0^{R_V(z)} dr\, r(-j_\theta)B_r \tag{27}$$

is the axial magnetic force of the azimuthal plasma current on the thruster magnetic circuit, here expressed as the reaction force of the applied magnetic field on the plasma currents, $j_\theta$.

For our simple geometric configuration,

$$F_{cham} = F_{pres} - F_{elec}$$

is the chamber (or internal) thrust,[28] while the magnetic thrust, $F_{mag}$, is exclusively external thrust. Particularizing $F_z(z)$ at sections A, B, E, and D yields the relations between the plasma momentum flow and the different contributions to thrust

$$\begin{aligned} F_{zB} &= F_{zA} - F_{elec}, \\ F_{zE} &= F_{zB} - D_W = F_{cham}, \\ F_{zD} &= F_{zE} + F_{mag} = F. \end{aligned} \tag{28}$$

The chamber thrust depends on the plasma temperature, $F_{cham}(T_e)$. For $B = 600$G, when lateral wall screening is large, the plasma "drag" on the lateral wall is negligible: $D_w/F_{cham} \simeq 0.01$. On the contrary, the negative contribution of the electric force is significant: taking $F_{pres} \simeq F_{zA}$ and the well-known Debye sheath solution for a floating wall, one has

$$\frac{F_{elec}}{F_{pres}} \simeq 1 - \frac{F_{zB}}{F_{zA}} \simeq 1 - \frac{2}{\sqrt{1 + \ln(m_i/(2\pi m_e))}} \simeq 0.38,$$

the last numerical value being for argon. Notice that if wall secondary-electron emission is important, $F_{elec}$ decreases but $F_{cham}$ does not change.

The magnetic thrust depends on both $T_e$ and $L_n$, but the ratio

$$\kappa_F = F_{mag}/F_{cham},$$

shown in Fig. 10(a) and called $\kappa_{noz}$ in Ref. 20, is nearly independent of $T_e$ (except for the weak dependence of ion magnetization on $T_e$), monotonic with $L_n$, and tending asymptotically to about 1. Therefore, we can write

$$F(T_e, L_n) \simeq F_{cham}(T_e)[1 + \kappa_F(L_n)]. \tag{29}$$

As an illustration, Fig. 11(a) plots the thrust of our simulated thruster versus the nozzle length and the plasma temperature. Recent experimental measurements on a HPT[17] yield values of $\kappa_F$ about 0.4-0.7, which agrees well with the results of Fig. 10(a).

It is worth to observe that the net force exerted by the plasma beam on the downstream plate P, $F_{plate}$, is the dynamic pressure on the plate *minus* the electric force due to positive electric charge in the adjacent Debye sheath,

$$F_{elec,P} = \pi\epsilon_0\int_0^{R_V(L_n)} dr\, r(d\phi/dz)_P^2.$$

Thus, one has

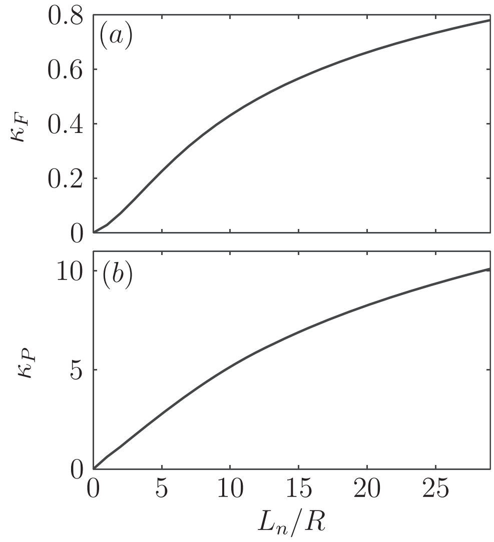


FIG. 10. (a) Thrust gain and (b) ion-power gain, versus nozzle length.

$$F_{plate} = F_{zP} + F_{elec,P} = F_{zD} = F. \tag{30}$$

This equivalence between the thrust on the thruster and the plasma force on a downstream plate has been validated experimentally, the average discrepancy being a 2%.[34] Notice that the equivalence is valid as long as (i) the plate presence does not modify substantially the upstream plasma beam, and (ii) there is no thrust contribution of the beam

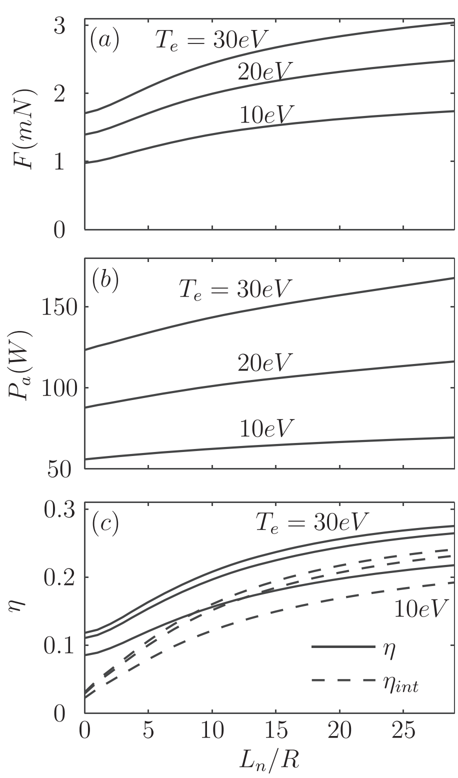


FIG. 11. Influence of nozzle length and plasma temperature on (a) thrust, (b) required absorbed power, (c, solid) thrust efficiency, and (c, dashed) internal efficiency. In all figures, curves are for $T_e = 10\,\text{eV}$, $20\,\text{eV}$, and $30\,\text{eV}$; in (c), both $\eta$ and $\eta_{int}$ increase with $T_e$. Results are for $B_0 = 600\,\text{G}$ and $\dot{m} = 0.1\text{mg/s}$.

downstream of the plate location. This last condition requires to know well the plasma behavior far-downstream, which is still an open problem.

The monotonic behavior of $\kappa_F(L_n)$ means that, for given $T_e$, the total thrust and the plasma momentum flow increase with the length of the nozzle region, Fig. 11(a). The question to be solved in Sec. V is whether that increment of plasma momentum flow with $L_n$ comes from an enhancement of the thrust efficiency or an increment on the power $P_a$ to be deposited into the plasma.

## V. THRUST EFFICIENCY

### A. Energy balance

The energy equation determines the plasma temperature $T_e$ in terms of the plasma absorbed power $P_a$, which is the dominant contribution to the energy balance of the discharge. Instead, Fruchtman *et al.*[27] claim that the power (i.e., energy) balance determines the plasma density, $n$, an assertion that we find incorrect: $n$ is indeed determined mainly by the mass flow $\dot{m}$, as the dimensionless solution for $n/n_0$, with $n_0 = \dot{m}/(m_i \pi R^2 c_s)$, of Sec. III shows clearly. Also, the setting of $T_e$ in the present externally heated discharge is totally different to the one taking place in a near-quiescent, self-sustaining glow discharge,[35] where the mass balance between volumetric ionization and wall recombination, yields $T_e$ as a function of $n_n R$ and the magnetic strength; in fact that function is Eq. (12) for the case $\nu_w \equiv n_n R_{ion}$.

The assumption of electron isothermality has the advantage that a *global* energy balance relates easily $P_a$ to the rest of discharge parameters. The discussion of the energy balance will be restricted here to the relation among $P_a$, $T_e$, and $L_n$, for given values of $B_0$, $\dot{m}$, $R$, and $L$.

The energy equation for the plasma, grouping contributions from all species can be expressed as

$$\nabla \cdot \dot{\boldsymbol{P}} = \boldsymbol{j} \cdot \boldsymbol{E} + \dot{P}_a - \dot{P}_{ion}. \tag{31}$$

Here,

$$\dot{\boldsymbol{P}}(z,r) = \frac{n_n}{2} m_i u_n^2 \boldsymbol{u}_n + \frac{n}{2}[m_i u_i^2 \boldsymbol{u}_i + (m_e u_{0e}^2 + 5T_e)\boldsymbol{u}_e] + \boldsymbol{q}_e \tag{32}$$

is the plasma power density, with $\boldsymbol{q}_e$ the electron heat flux; $\dot{P}_a$ is the absorbed power density; and

$$\dot{P}_{ion} = E'_{ion} n n_n R_{ion} \equiv \nabla \cdot (E'_{ion} n \boldsymbol{u}_i)$$

groups energy losses due to ionization and excitation, with $E'_{ion}(T_e)$ an effective ionization energy defined in the Appendix. In the nozzle, the contribution of neutrals to $\dot{\boldsymbol{P}}$, Eq. (32), is negligible, and the contribution of the electron azimuthal energy $m_e u_{0e}^2/2$ must be kept small for the nozzle model being consistent;[10,21] in the simulations to follow it will be kept below 10%.

Making use of $\nabla \cdot \boldsymbol{j} = 0$, the work of the electric field satisfies $\boldsymbol{j} \cdot \boldsymbol{E} = -\nabla \cdot (\phi \boldsymbol{j})$ and the energy equation takes the conservation form

$$\nabla \cdot [\dot{\boldsymbol{P}} + E'_{ion} n \boldsymbol{u}_i + \phi \boldsymbol{j}] = \dot{P}_a. \tag{33}$$

Integrating this equation over the whole plasma domain, limited by chamber walls A and W, the nozzle/vacuum edge V, and the downstream plate P, the energy conservation balance can be expressed as

$$P_{ion} + P_{wall} + P_{beam} = P_a. \tag{34}$$

On the left-hand side, the contributions of ionization (plus radiation), wall heating, and downstream beam are

$$\begin{aligned} P_{ion} &= E'_{ion} \dot{m}_{iT}/m_i, \\ P_{wall} &= P_W + P_A, \\ P_{beam} &= P_P, \end{aligned} \tag{35}$$

respectively. Here,

$$\begin{aligned} P_W = P_Q &= 2\pi R \int_{-L}^{0} dz \boldsymbol{1}_r \cdot \dot{\boldsymbol{P}}(z,R), \\ P_A = P_B &= -2\pi \int_0^R dr\, r \boldsymbol{1}_z \cdot \dot{\boldsymbol{P}}(z_B, r), \\ P_P = P_D = P_E &= 2\pi \int_0^{R_V(z_D)} dr\, r \boldsymbol{1}_z \cdot \dot{\boldsymbol{P}}(z_D, r), \end{aligned} \tag{36}$$

represent radial and axial energy flows at different surfaces. The equalities $P_A = P_B$, $P_Q = P_W$, and $P_D = P_P$ express that there is no energy spent by the current-free plasma in sheaths AB, QW, and DP, just an energy transfer from electrons to ions. Then, the equality $P_E = P_D = P_{beam}$ also means that there are no energy sources in the nozzle.

The chamber model determines $P_{ion}(T_e)$ and $P_{wall}(T_e)$. Then, the nozzle model yields

$$P_{beam} = P_i(z) + P_e(z) = \text{const} \tag{37}$$

with

$$\begin{aligned} P_i(z) &= \pi \int_0^{R_V(z)} dr\, r n m_i u_i^2 u_{zi}, \\ P_e(z) &\simeq \pi \int_0^{R_V(z)} dr\, r (5 T_e n u_{ze} + 2 q_{ze}), \end{aligned} \tag{38}$$

$m_e u_0^2 \ll 2T_e$ was assumed. Equation (37) expresses the transfer of electron "internal" energy to ion "kinetic" energy along the nozzle.

The nozzle model determines $P_i(z)$, with $P_i(0)$ corresponding to the sonic ion flow at section E. In fact and as for $\kappa_F$, the ratio

$$\kappa_P = P_i(z)/P_i(0) - 1$$

is almost independent of $T_e$ (constant), and the parametric dependence of the ion power can be expressed as

$$P_{iD}(T_e, L_n) \simeq P_{iE}(T_e)[1 + \kappa_P(L_n)]. \tag{39}$$

Figure 10(b) plots $\kappa_P(L_n)$, which is approximately proportional to the square of the local $r$-averaged Mach number in the nozzle; thus $\kappa_P = 10$ corresponds to a Mach number of $\approx 3$.

The electron energy flow is the sum of enthalpy and heat flows. For $T_e = \text{const}$, the enthalpy flow, $(5/2) T_e \dot{m}_{iE}/m_i$, is constant along the nozzle, and the non-zero electron heat flux, $q_{ze}$, can be determined directly only at the plate sheath edge D. The fluid-to-kinetic correspondence for energy fluxes (of a near-Maxwellian population) at the edge of a collisionless sheath yields[36]

$$\frac{5}{2} T_e n u_{ze} + q_{ze} = \left(2 + \frac{1}{2} \ln \frac{m_i}{2\pi m_e}\right) T_e n u_{ze}, \tag{40}$$

and, integrating on section D,

$$P_{eD}(T_e) = \left(2 + \frac{1}{2} \ln \frac{m_i}{2\pi m_e}\right) T_e \frac{\dot{m}_{iE}}{m_i}. \tag{41}$$

Substituting Eqs. (39) and (41) in Eq. (37), the parametric dependence of the beam power becomes

$$P_{beam}(T_e, L_n) = P_{eD}(T_e) + P_{iE}(T_e)[1 + \kappa_P(L_n)]. \tag{42}$$

Since $P_{iE} \simeq T_e \dot{m}_{iE}/(2m_i)$, one has

$$P_{iE}(T_e)/P_{eD}(T_e) \simeq \left(4 + \ln \frac{m_i}{2\pi m_e}\right)^{-1},$$

so, at the chamber exit, only a small fraction (about one-fifteenth for argon) of the plasma energy is deposited on the (sonic) ion flow.

Returning to the energy balance, Eq. (34), the absorbed power $P_a$ required to create and expand a plasma of temperature $T_e$ along a nozzle of length $L_n$ satisfies the functional relation

$$P_a = P_{ion}(T_e) + P_{wall}(T_e) + P_{beam}(T_e, L_n) \tag{43}$$

(for $B_0$ and $\dot{m}$ given). Figure 11(b) plots $P_a(L_n)$ for different plasma temperatures. For $T_e$ given, one has

$$P_a(L_n) - P_a(0) = P_{iD}(L_n) - P_{iE} = P_{eD}(0) - P_{eD}(L_n).$$

Therefore, for given $T_e$, the increase of absorbed power with $L_n$ is supplied to the beam at the chamber exit as an increase of the electron heat flow. On the contrary, if the absorbed power is kept constant, and the plate location is moved, it is evident from Fig. 11(b) that, as $L_n$ increases, the plasma temperature (determined globally) decreases. The isothermal electron model and its consequences are further discussed in Sec. V C.

### B. Partial efficiencies

Thrust efficiency is defined as

$$\eta = F^2 / 2\dot{m} P_a. \tag{44}$$

Figure 11(c) shows that thrust efficiency is enhanced when either $T_e$ or $L_n$ are increased; both cases imply an increase of the absorbed power. For our present thruster and plasma model, thrust efficiency remains below 30%. In order to understand this relatively modest performance figure, we evaluate next how the different phenomena taking place on the discharge affect the thrust efficiency.

Thrust efficiency is based on magnitudes external to the plasma discharge, which facilitates its computation. Alternatively, plasma beam properties are used by Sutton[37] in the definition of the thruster internal efficiency,

$$\eta_{int} = P_{ziD}/P_a, \tag{45}$$

with

$$P_{ziD} = \pi \int_0^{R_V(L_n)} dr\, r n m_i u_{zi}^3(L_n, r)$$

the flow of ion axial kinetic energy at final section D. The two efficiencies coincide only if the beam expansion is complete. The internal efficiency can be factorized as

$$\eta_{int} = \eta_{cham}\eta_{con}\eta_{div}, \tag{46}$$

with

$$\begin{aligned} \eta_{cham} &= P_{beam}/P_a = 1 - \epsilon_{ion} - \epsilon_{wall}, \\ \eta_{con} &= P_{iD}/P_{beam}, \\ \eta_{div} &= P_{ziD}/P_{iD}, \end{aligned} \tag{47}$$

partial efficiencies related to chamber processes, internal-to-kinetic energy conversion in the nozzle, and the beam or plume divergence, respectively; $\epsilon_{ion} = P_{ion}/P_a$ and $\epsilon_{wall} = P_{wall}/P_a$ are the relative losses due to ionization and wall heating.

Figure 12(a) shows for a long nozzle ($L_n/R = 30$) the dependence on $T_e$ of $\epsilon_{ion}$, $\epsilon_{wall}$, $\eta_{int}$, and $\eta$; the two other efficiencies are independent of $T_e$, being $\eta_{con} \simeq 0.44$ and $\eta_{div} \simeq 0.95$. The back wall contributes the most to $\epsilon_{wall}$ and its increase with $T_e$ is due to $P_{wall} \propto T_e^{3/2}$. The decrease of $\epsilon_{ion}$ when $T_e$ increases is due to the transition to the high-ionization region and the decrease of excitation collisions. The positive difference between $\eta$ and $\eta_{int}$ for large $T_e$ is due to the electron contribution to thrust not having a correspondence on $\eta_{int}$; the negative difference at low $T_e$ is due to the poor propellant utilization. Figure 12(b) plots the same partial efficiencies versus the absorbed power instead of $T_e$. The difference between both groups of curves is summarized in the fact that increments of $P_a$ are spent in ionizing more gas, at low power, and in heating the plasma, at high power.

Figure 12 yields that the maximum thrust efficiency of our modeled thruster is below 30%. We are now in conditions to identify the main causes reducing efficiency (excepting, of course, those related to plasma-wave interaction). First, it is clear that the thruster must operate in the high ionization regime. For instance, for $L_n/R = 30$ and $P_a = 150$ W, ionization-plus-radiation losses amount only to a 10% of the efficiency loss, according to Fig. 12(b). The same Figure states that a 30% of the efficiency loss is due to energy losses at the chamber back-wall. Therefore, screening adequately that wall (without affecting much the rest of the chamber)

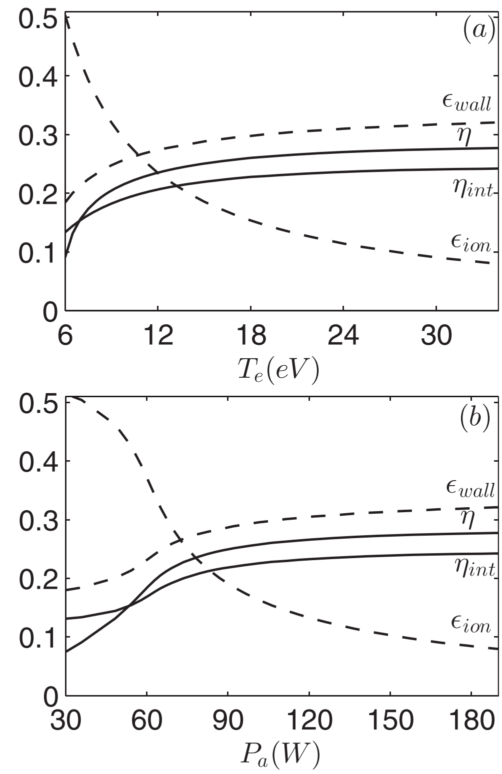


FIG. 12. Dependence of (solid lines) thrust and internal efficiencies and (dashed lines) ionization and wall losses with (a) $T_e$ and (b) $P_a$, for $L_n = 30$ cm, $B_0 = 600$G, and $\dot{m} = 0.1$ mg/s.

would yield $\eta_{cham} \sim 80\%$ instead of 60%. The rest of efficiency losses takes place in the nozzle. First, the beam-divergence efficiency is excellent ($\eta_{div} \simeq 95\%$), but this can be due to the limited extension of our nozzle region. Further studies on the plasma detachment region are needed to confirm the behavior of $\eta_{div}$. Second, the efficiency loss caused by the conversion of electron-to-ion energy is poor, $\eta_{con} \simeq 44\%$. This result is very dependent on the electron equation of state we have assumed, so a discussion on this subject is very pertinent.

### C. On the electron equation of state

An isothermal electron population has been assumed here for both chamber and nozzle models. Isothermality was used in previous 1D magnetic-nozzle models,[9] and the (isothermal) Boltzmann relation is very often invoked in plasma plume models.[38] Except for the small drift flows into the chamber walls and the downstream plume, electrons constitute a population well confined both electrostatically and magnetically. This promotes that, in a stationary situation, electrons approach thermodynamic equilibrium, thus supporting isothermality.

Fruchtman *et al.*,[27] who study only the chamber region of a HPT, assume isothermality inside the chamber, but impose an adiabatic condition (i.e., zero heat flow) at the chamber exit. This would be consistent with an adiabatic expansion of the plasma beam along the magnetic nozzle, similar to the one taking place for a hot dense gas in a solid nozzle.[37] However, the plasma beam of a HPT is tenuous and high-collisionality cannot be claimed to support local thermodynamic equilibrium and isentropic expansion.

The choice isothermal versus adiabatic has important consequences on the downstream plasma expansion, the energy balance, and the thruster internal efficiency. For an isothermal, collisionless magnetic nozzle, we have found that: the ambipolar electric potential decreases without bound (as $L_n$ increases); the electron enthalpy flow is constant along the nozzle, while the electron heat flow at the chamber exit increases as $L_n$ increases (in order to balance the total gain of ion kinetic energy in the nozzle); and the electron-to-ion energy conversion efficiency is poor.

On the contrary, from the similarity with hot-gas physics, in the adiabatic expansion of a collisional plasma, one would have that: the ambipolar electric field tends to zero downstream; the electron heat flow at the chamber exit and within the nozzle is zero; the gain in ion energy is balanced by the decrease of the electron enthalpy; and the energy conversion efficiency is high. A welcome consequence of adiabacity is that the beam power is known independently of the expansion in the nozzle:[27,39] $P_{beam}(T_e) \simeq 3T_{eE}\dot{m}_{iE}/m_i$. Figure 9 of Ref. 39 shows graphically the relation $P_a(T_e)$ in the adiabatic limit.

Although the non-local character of the electron energy transport in our isothermal model is more suitable for a near-collisionless population, we acknowledge that both limit cases, isothermal and adiabatic, are crude models for the equation of state of a collisionless electron population. Indeed, there is some experimental evidence of plasma cooling in magnetized and unmagnetized plumes.[38,40] Also, non-local collisionless cooling of electrons has been studied theoretically with a quasi-1D time-dependent model by Arefiev and Breizman.[41] Cooling would be caused by the partial depletion of a Maxwellian distribution function along a divergent magnetic nozzle with a traveling rarefaction wave acting as downstream "reflection boundary." Martínez-Sánchez and Ahedo[42] analyzed the partially equivalent problem of a steady-state quasi-1D ion flow in a convergent magnetic geometry, and indeed obtained spatially varying *parallel* and *perpendicular* temperatures and *non-zero* heat flows. These two works would show the way for analyzing non-local collisionless cooling of electrons and the corresponding equation of state in a 2D stationary divergent flow.

## VI. CONCLUSIONS

A 2D fluid model of the plasma flow inside the magnetized chamber of a helicon thruster has been developed, with assumptions based on expected ranges of plasma density and temperature. Ionization, confinement, and 2D plasma flow have been discussed in terms of design and operational parameters, i.e., chamber dimensions, injected gas flow, magnetic field strength, and plasma temperature, the last one a function of the plasma absorbed power. Analytical solutions for an ideal, near-collisionless plasma have been derived, and provide simple scaling laws for the plasma parametric response. Optimal values of design and operational parameters that maximize propellant utilization and production efficiency have been investigated.

The chamber model has then been matched with an existing nozzle model. The whole model provides a complete picture of the fluid-dynamic processes of the plasma discharge in a helicon thruster (heating, ionization, confinement, and acceleration) and the capability of assessing thruster performances, such as thrust, power balance, and thruster efficiencies, assuming isothermal electrons. In particular, the analysis of the momentum and energy equations of the whole plasma has determined (i) the thermal, electric, and magnetic contributions to thrust, (ii) the power conversion between ions and electrons in chamber and nozzle, and (iii) the power distribution among beam power, ionization losses, and wall losses.

Thrust and internal efficiencies have been evaluated, obtaining maximum values below 30% for the cases simulated here. The main causes of inefficiency are two: the deficient magnetic screening of the chamber walls (mainly the rear wall for a near axial magnetic field) and the incomplete plasma expansion in the nozzle (at least for isothermal electrons).

Indeed, that expansion depends on the thermodynamics of collisionless electrons in the nozzle divergent geometry, which is bad known and thus constitutes the most uncertain aspect when determining thruster performances. Isothermal and polytropic equations of state are shown to yield rather different plasma responses. For an isothermal flow, we were forced to place a downstream collecting plate in order to close the energy balance, and the plasma temperature depends on both the absorbed power and the nozzle region length. Far downstream plasma response is also affected by detachment from the nozzle.

A complete model of the plasma discharge in a helicon thruster will match the present fluid-dynamic model with a 2D model of the wave-plasma interaction and energy transfer. It is known from simple wave-plasma models that antenna-plasma coupling is more efficient within particular ranges of plasma density and magnetic strength and could be more critical for efficient thruster operation than the flow-related phenomena analyzed here. The wave-plasma interaction model should also assess whether (or under which conditions) suprathermal electrons are created. This can be instrumental in the formation of double-layer class structures in the supersonic plasma flow.

Finally, in search of tractability, several simplifications have been adopted in the fluid model, such as the 1D magnetic topology in the chamber, the absence of double-charged ions (which are not insignificant in the expected range of $T_e$), and the approximate separation between radial and axial dynamics. These limitations should not alter the main trends of the plasma response here but reduce the accuracy of the results. Their overcoming requires presumably to opt for particle-in-cell or hybrid schemes, instead of fluid ones, as it has been already the case with other plasma thrusters.[43,44]

## ACKNOWLEDGMENTS

The authors thank Mario Merino for providing plasma simulations of the magnetic nozzle stage. Partial versions of this work were presented in two Conference papers.[39,45] The research has been sponsored by Spain's R&D National Plan

(Project AYA-2010-61699) and FPU scholarship program. Additional support has been provided by the Air Force Office of Scientific Research, Air Force Material Command, USAF, under Grant No. FA8655-12-1-2043. The U.S. Government is authorized to reproduce and distribute reprints for Governmental purpose notwithstanding any copyright notation thereon.

## APPENDIX: COLLISION RATES

The expressions proposed below for the different collision rates are reasonable approximations for the purposes of this work. The rates for ionization, electron-neutral collisions, electron-ion collisions, and ion-neutral collisions are, respectively,

$$R_{ion}(T_e) = \sqrt{\frac{8T_e}{\pi m_e}}\sigma_{ion}\left(1 + \frac{T_e E_{ion}}{(T_e + E_{ion})^2}\right)\exp\left(-\frac{E_{ion}}{T_e}\right), \tag{A1}$$

$$R_{en}(T_e) = \sqrt{\frac{8T_e}{\pi m_e}}\sigma_{en}, \tag{A2}$$

$$R_{ei}(T_e, n_e) = \left(\frac{T_e}{1\,\text{eV}}\right)^{-3/2} \ln\Lambda(T_e, n_e)\cdot 9.2\cdot 10^{-14}\text{m}^3\text{s}^{-1}, \tag{A3}$$

with $E_{ion}$ the first ionization energy. For ion-neutral collisions and $c_{in} = |\boldsymbol{u}_i - \boldsymbol{u}_n|$, we have

$$R_{in}(c_{in}) = c_{in}(k_2 - k_1\log_{10}c_{in})^2. \tag{A4}$$

The constants involved in the above expressions are gas-dependent. For argon, they are $E_{ion} = 15.76$ eV, $\sigma_{ion} = 2.8\cdot 10^{-20}\,\text{m}^2$, $\sigma_{en} = 15\cdot 10^{-20}\,\text{m}^2$, $k_2 = 10.5\cdot 10^{-10}\,\text{m}$, and $k_1 = 1.67\cdot 10^{-10}\,\text{m}$ (if $c_{in}$ is in m/s).

For $T_e = \text{const}$ and a given gas, $R_{ion}$, $R_{en}$, and $R_{in,s} = R_{in}(c_s)$ are constant; $R_{ei}$ is a constant too if an average value is used for $\ln\Lambda(n_e, T_e)$. Observe that the non-linear expression used for $R_{in}$ correspond to the high-pressure case of Fruchtman *et al.*,[27] but, even for this case, ion-neutral collisions will be found negligible in the desired operation range.

Excitation collisions are taken into account through the effective ionization energy $E'_{ion}(T_e) = E_{ion}\alpha_{ion}(T_e)$ with $\alpha_{ion}$ the ionization cost factor. From Dugan,[46] a fitting formula for argon is

$$\alpha_{ion}(T_e) \approx 1.4 + 0.4\exp(0.7\,E_{ion}/T_e). \tag{A5}$$


[1] T. Ziemba, J. Carscadden, J. Slough, J. Prager, and R. Winglee, in *41th AIAA/ASME/SAE/ASEE Joint Propulsion Conference & Exhibit*, AIAA Paper No. 2005-4119, 2005.

[2] M. West, C. Charles, and R. Boswell, J. Propul. Power **24**, 134 (2008).

[3] O. Batishchev, IEEE Trans. Plasma Sci. **37**, 1563 (2009).

[4] D. Pavarin *et al.*, in *31th International Electric Propulsion Conference*, IEPC Paper No. 2009-205, 2009.

[5] E. Ahedo, "Plasma dynamics in a helicon thruster," in *EUCASS Advances in Aerospace Sciences*, Progress in Propulsion Physics Vol. IV, edited by L. DeLuca, C. Bonnal, O. Haidn, and S. Frolov (Torus Press, 2013), pp. 337–354.

[6] K. Shamrai, Y. V. Virko, V. F. Virko, and A. I. Yakimenko, in *42th AIAA/ASME/SAE/ASEE Joint Propulsion Conference & Exhibit*, AIAA Paper No. 2006-4845, 2006.

[7] D. Palmer, M. Walker, M. Manente, J. Carlsson, C. Bramanti, and D. Pavarin, in *44th AIAA/ASME/SAE/ASEE Joint Propulsion Conference & Exhibit*, AIAA Paper No. 2008-4925, 2008.

[8] E. Ahedo, Phys. Plasmas **16**, 113503 (2009).

[9] S. Andersen, V. Jensen, P. Nielsen, and N. D'Angelo, Phys. Fluids **12**, 557 (1969).

[10] E. Ahedo and M. Merino, Phys. Plasmas **17**, 073501 (2010).

[11] F. Chen, Plasma Phys. Controlled Fusion **33**, 339 (1991).

[12] R. Boswell, Plasma Phys. Controlled Fusion **26**, 1147 (1984).

[13] K. Shamrai and V. Taranov, Plasma Phys. Controlled Fusion **36**, 1719 (1994).

[14] M. Lieberman and A. Lichtenberg, *Principles of Plasma Discharges and Materials Processing* (Wiley-Blackwell, 2005).

[15] G. Parissenti *et al.*, in *Proceedings of Space Propulsion 2010*, SP2010-1841086 (European Space Agency, Noordwijk, The Netherlands), 2010.

[16] E. Ahedo, Plasma Phys. Controlled Fusion **53**, 124037 (2011).

[17] K. Takahashi, T. Lafleur, C. Charles, P. Alexander, and R. Boswell, Phys. Rev. Lett. **107**, 235001 (2011).

[18] L. Williams and M. Walker, in *47th AIAA/ASME/SAE/ASEE Joint Propulsion Conference & Exhibit*, AIAA Paper No. 2011-5893, 2011.

[19] S. Pottinger, V. Lappas, C. Charles, and R. Boswell, J. Phys. D: Appl. Phys. **44**, 235201 (2011).

[20] E. Ahedo and M. Merino, Phys. Plasmas **18**, 053504 (2011).

[21] M. Merino and E. Ahedo, Phys. Plasmas **19**, 083501 (2012).

[22] M. Merino and E. Ahedo, in *48th AIAA/ASME/SAE/ASEE Joint Propulsion Conference & Exhibit*, AIAA Paper No. 2012-3843, 2012.

[23] E. Ahedo and M. Martínez-Sánchez, Phys. Rev. Lett. **103**, 135002 (2009).

[24] E. Ahedo, Phys. Plasmas **18**, 033510 (2011).

[25] M. Merino and E. Ahedo, Phys. Plasmas **20**, 023502 (2013).

[26] E. Ahedo, J. Gallardo, and M. Martínez-Sánchez, Phys. Plasmas **10**, 3397 (2003).

[27] A. Fruchtman, G. Makrinich, and J. Ashkenazy, Plasma Sources Sci. Technol. **14**, 152 (2005).

[28] A. Fruchtman, IEEE Trans. Plasma Sci. **36**, 403 (2008).

[29] E. Ahedo, Phys. Plasmas **18**, 103506 (2011).

[30] L. Tonks, Phys. Rev. **56**, 360 (1939).

[31] M. Merino and E. Ahedo, in *Proceedings of Space Propulsion 2010*, SP2010-1841391 (European Space Agency, Noordwijk, The Netherlands), 2010.

[32] K. Schoenberg, R. Gerwin, R. Moses, J. Scheuer, and H. Wagner, Phys. Plasmas **5**, 2090 (1998).

[33] D. Chavers and F. Chang-Díaz, Rev. Sci. Instrum. **73**, 3500 (2002).

[34] B. Longmier, B. Reid, A. Gallimore, F. Chang-Díaz, J. Squire, T. Glover, G. Chavers, and E. Bering III, J. Propul. Power **25**, 746 (2009).

[35] R. Franklin, *Plasma Phenomena in Gas Discharges* (Clarendon Press, Oxford, 1976).

[36] E. Ahedo and D. Escobar, Phys. Plasmas **15**, 033504 (2008).

[37] G. Sutton and O. Biblarz, *Rocket Propulsion Elements* (Wiley, 2010).

[38] I. D. Boyd, J. Spacecr. Rockets **38**, 381 (2001).

[39] E. Ahedo, in *31th International Electric Propulsion Conference*, IEPC Paper No. 2009-193, 2009.

[40] K. Dannenmayer, S. Mazouffre, M. Merino, and E. Ahedo, in *48th AIAA/ASME/SAE/ASEE Joint Propulsion Conference & Exhibit*, AIAA Paper No. 2012-4117, 2012.

[41] A. Arefiev and B. Breizman, Phys. Plasmas **15**, 042109 (2008).

[42] M. Martínez-Sánchez and E. Ahedo, Phys. Plasmas **18**, 033509 (2011).

[43] F. Parra, E. Ahedo, M. Fife, and M. Martínez-Sánchez, J. Appl. Phys. **100**, 023304 (2006).

[44] F. Taccogna, S. Longo, M. Capitelli, and R. Schneider, Contrib. Plasma Phys. **47**, 635 (2007).

[45] J. Navarro, M. Merino, and E. Ahedo, in *48th AIAA/ASME/SAE/ASEE Joint Propulsion Conference & Exhibit*, AIAA Paper No. 2012-3840, 2012.

[46] J. Dugan and R. Sovie, Tech. Rep. NASA TN D-4150, 1967.